A&A 529, A124 (2011)
DOI: 10.1051/0004-6361/201016150

Astronomy & Astrophysics

Redshift evolution of the 1.4 GHz volume averaged radio luminosity function in clusters of galaxies

M. W. Sommer[1], K. Basu[1,2], F. Pacaud[1], F. Bertoldi[1], and H. Andernach[1,⋆]

[1] Argelander-Institut für Astronomie, Auf dem Hügel 71, 53121 Bonn, Germany
e-mail: mnord@astro.uni-bonn.de
[2] Max Planck-Institut für Radioastronomie, Auf dem Hügel 69, 53121 Bonn, Germany

Received 15 November 2010 / Accepted 15 March 2011

ABSTRACT

By cross-correlating large samples of galaxy clusters with publicly available radio source catalogs, we construct the volume-averaged radio luminosity function (RLF) in clusters of galaxies, and investigate its dependence on cluster redshift and mass. In addition, we determine the correlation between the cluster mass and the radio luminosity of the brightest source within 50 kpc from the cluster center. We use two cluster samples: the optically selected maxBCG cluster catalog and a composite sample of X-ray selected clusters. The radio data come from the VLA NVSS and FIRST surveys. We use scaling relations to estimate cluster masses and radii to get robust estimates of cluster volumes. We determine the projected radial distribution of sources, for which we find no dependence on luminosity or cluster mass. Background and foreground sources are statistically accounted for, and we account for confusion of radio sources by adaptively degrading the resolution of the radio source surveys. We determine the redshift evolution of the RLF under the assumption that its overall shape does not change with redshift. Our results are consistent with a pure luminosity evolution of the RLF in the range $0.1 \leq z \leq 0.3$ from the optical cluster sample. The X-ray sample extends to higher redshift and yields results also consistent with a pure luminosity evolution. We find no direct evidence of a dependence of the RLF on cluster mass from the present data, although the data are consistent with the most luminous sources only being found in high-mass systems.

Key words. galaxies: clusters: general – radio continuum: galaxies – galaxies: active – galaxies: evolution

1. Introduction

The study of radio sources inside galaxy clusters is becoming increasingly important in the context of large-area Sunyaev-Zel'dovich effect (SZE, Sunyaev & Zeldovich 1972; Birkinshaw 1999) cluster surveys (e.g. Schwan et al. 2003; Ho et al. 2009; Vanderlinde et al. 2010; Muchovej et al. 2010), especially in the case of single-frequency SZE surveys and where the resolution is matched with the typical cluster size. Powerful radio sources are generally associated with early type galaxies, and as the latter preferentially reside in clusters, it is expected that radio sources can alter the SZE decrement in both position an depth.

Apart from contamination of SZE surveys, a study of the radio-loud population of AGN inside galaxy clusters sheds light on the interaction between cluster cooling flows and AGN heating/feedback scenarios (e.g. Martini et al. 2009). Analyzing the radio properties of galaxy clusters can provide direct evidence of heating of the intra-cluster medium (ICM) by AGN through various stages of cluster formation (e.g. Hart et al. 2009).

Three pieces of information are crucial to assess the radio source contamination of SZE observations: (1) the distribution of sources as a function of projected distance from the cluster center; (2) the brightness distribution of sources and its redshift evolution; and (3) the spectral energy distributions (SEDs) of the sources. A convenient way of dealing with the first two points is to construct a radio luminosity function (RLF), i.e. the number density of sources as a function of luminosity, averaged over the cluster volume. This is the objective of the present paper.

Ledlow & Owen (1996) first constructed the RLF for radio galaxies in clusters using a 20 cm VLA survey of Abell clusters. Similar studies were carried out by Reddy & Yun (2004) for seven nearby galaxy clusters, and by Massardi & De Zotti (2004) for a much larger sample of 951 Abell clusters at low redshifts. Stocke et al. (1999) used a sample of 19 X-ray selected clusters at $0.2 < z < 0.8$ to constrain the evolution of radio galaxies, and comparing their results with those of Ledlow & Owen (1996), they found no evidence for an evolution of the radio-loud AGN population. Similar conclusions were drawn by Coble et al. (2007) using a sample of massive clusters detected through the SZE decrement at 30 GHz. Although Branchesi et al. (2006) found indications of redshift evolution in both slope and amplitude of the cluster RLF when comparing VLA observations of a sample of 18 X-ray selected clusters with the results of Stocke et al., no definitive conclusions were drawn on the RLF redshift evolution. Gralla et al. (2010) studied the radio source population in a sample of 618 optically selected galaxy clusters in the redshift range $0.35 < z < 0.95$ and found no significant redshift dependence in the number density of radio sources.

Recent high-resolution X-ray imaging of clusters have provided evidence that the AGN fraction inside clusters rapidly evolves with redshift (Eastman et al. 2007; Martini et al. 2009). These results are affected by small number statistics, since the AGN fraction in any single cluster is very small and can also vary with other cluster properties, such as the velocity dispersion

⋆ *Permanent address*: Departamento de Astronomía, Universidad de Guanajuato, AP 144, Guanajuato CP 36000, Mexico.

(Sivakoff et al. 2008). The volume-averaged radio luminosity function is therefore expected to be a more robust indicator of redshift evolution. Correlating X-ray selected clusters with optical and IR selected AGN, Galametz et al. (2009) confirmed that the AGN excess near cluster centers increases with redshift. A parametric modeling of this positive evolution, which can be used to predict the radio AGN contamination in SZE cluster surveys, was not considered in these studies.

Lin & Mohr (2007, hereafter LM07) used a sample of 573 X-ray selected clusters to estimate masses and virial radii, yielding a more physically meaningful cluster volume for the RLF than obtained when using a constant cluster radius. We adopt that method in this paper. LM07 found a narrow radial distribution of radio sources, which we reproduce in this work.

This study focuses on the redshift evolution of the RLF and its decoupling from a possible dependence on cluster mass. We use publicly available radio source catalogs at 1.4 GHz to identify radio sources associated with clusters of galaxies in a large sample of optically selected clusters (Koester et al. 2007) and a composite sample of ROSAT selected X-ray clusters. Studies of radio point sources in clusters at higher frequencies were carried out by, e.g., Cooray et al. (1998), Coble et al. (2007) and Lin et al. (2009), and the extrapolation of the RLF from 1.4 GHz to frequencies relevant for SZE surveys was investigated by, e.g., Massardi & De Zotti (2004) and by LM07. These two aspects are not pursued in this work.

This paper is organized as follows: in Sect. 2 we describe the samples of radio sources and cluster of galaxies. We discuss the estimation of cluster masses from observable properties for clusters selected from optical and X-ray cluster catalogs, and describe how radio luminosities are derived from flux densities. The radial density profile of radio sources associated with clusters of galaxies is discussed in Sect. 3. In Sect. 4, we investigate the correlation between cluster mass and the luminosity of the brightest radio source in the central region of the cluster. The main part of the paper is Sect. 5, where the 1.4 GHz volume-averaged radio luminosity in galaxy clusters is derived from our sample. The method of computing the RLF is described, and the statistical treatment of sources not associated with the clusters is discussed. Confusion of sources is discussed, and the redshift evolution of the RLF is derived. We summarize our main results and offer our conclusions in Sect. 6.

Where not otherwise noted, we use the cosmological parameters from the WMAP 5-year cosmology (Komatsu et al. 2009) with $h = 0.705$, $\Omega_m h^2 = 0.136$ and $\Omega_\Lambda = 0.726$.

2. Cluster and radio source samples

In this section we describe the galaxy cluster samples and 1.4 GHz radio source catalogs used in this paper.

2.1. Cluster samples

To demonstrate a redshift evolution of the RLF in the best possible way, we select clusters with a wide range of redshifts from publicly available optical and X-ray surveys. To make robust estimates of the volume averaged RLF, we derive cluster masses and radii using scaling relations. The mass within a region whose mean density is 200 times the critical density of the universe at the cluster redshift, M_{200}, has been found to be a good estimator of the virial mass (e.g. White 2001), and is used here together with the corresponding radius, r_{200}, which we use to define the typical scale of the cluster.

Table 1. Our composite X-ray cluster sample.

Catalog	Number of clusters	Limiting flux (erg s^{-1} cm^{-2})
REFLEX	447	2.1e-12
NORAS	371	1.2e-12
160deg2	221	8.0e-14
400deg2	242	1.4e-13
WARPS1+2	124	8.0e-14
MACS($z > 0.5$)	12	7.0e-13

Notes. The third column is the effective flux limit, in the [0.5−2] keV energy band, estimated from our recomputed source parameters.

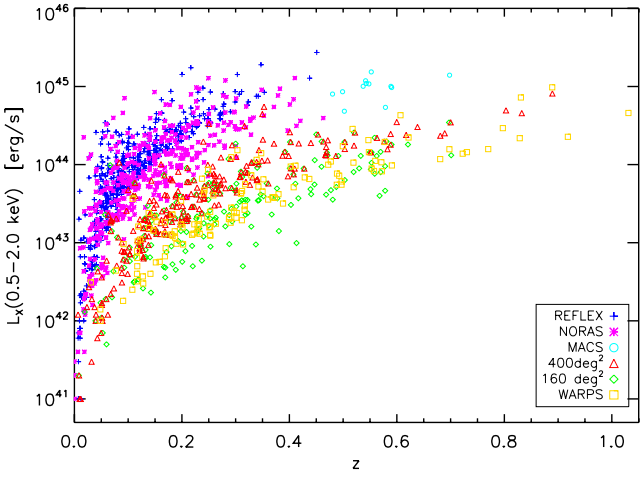

Fig. 1. Distribution of X-ray selected clusters of galaxies in the $L_X - z$ plane.

2.1.1. Description of the samples

Because of its large sample size, we use as our main sample the optical maxBCG catalog (Koester et al. 2007), which contains a total of 13 823 clusters extracted from the Sloan Digital Sky Survey (SDSS). This is by far the largest homogeneous publicly available cluster sample, and its redshift range $0.1 < z < 0.3$, corresponding to approximately 2.5×10^9 years of cosmic time, is large enough to allow an investigation of the redshift dependence of the RLF.

To allow a comparison with X-ray selected clusters, we have gathered in one large sample most of the published cluster detections from the ROSAT mission. Data products from this satellite remain the reference to date since only few new massive systems have been reported from more recent observatories. Our source list includes the ROSAT all-sky survey catalogs from NORAS and REFLEX (Böhringer et al. 2000, 2004), and some serendipitous catalogs extracted from the archives of pointed observations: the 160 deg^2 (Vikhlinin et al. 1998), the 400 deg^2 (Burenin et al. 2007) and WARPSI/II (Burenin et al. 2007; Horner et al. 2008) catalogs. We also added the complete sample of 12 high redshift very luminous systems of Ebeling et al. (2007). In total this yields 1177 X-ray selected clusters. The number of clusters from the respective catalogs and the corresponding flux limits are given in Table 1. Mixing these catalogs enables us to sample a large fraction of the $L_X - z$ plane, as can be seen in Fig. 1.

2.1.2. Cluster masses and radii

For the maxBCG sample, we estimate halo masses from the scaled richness parameter $n_{\rm gal}^{R200}$. Koester et al. (2007) and

Table 2. Cluster sample selection criteria.

	Main sample	maxBCG	X-ray	
1	clusters in main sample	13 823	1177	
2	clusters with sufficient separation	12 846	1121	
	Sub-sample		**high-z**	**low-z**
	Redshift range	$0.1 \le z \le 0.3$	$0.1 \le z \le 1.26$	$0.05 < z < 0.12$
3	Clusters within redshift range	12 846	690	292
4	Clusters with $M > 5 \times 10^{13}\ M_\odot$	12 522	674	275
5	clusters with NVSS coverage[a]	12 475	596	218
6	clusters with FIRST coverage[a]	11 812	273	75

Notes. The selection is cumulative in the sense that in rows 3−4, each row assumes all the conditions of the previous rows. Rows 5 and 6 assume all the conditions in rows 2−4. The low-z X-ray sample is used only to constrain the mass dependence of the RLF (Sect. 5.3.3). Where not explicitly stated otherwise, the high-redshift samples are used in this paper.
[(a)] Excluding regions with abnormally high or abnormally low source counts (see text).

Becker et al. (2007) found that this measure correlates well with the galaxy velocity dispersion, and thus also with halo mass. Indeed, Andreon & Hurn (2010) found that optical richness and X-ray luminosity perform similarly well in predicting cluster masses. The relation between $n_{\rm gal}^{R200}$ and M_{200} has been extensively studied, both using weak lensing (Johnston et al. 2007; Mandelbaum et al. 2008; Sheldon et al. 2009; Rozo et al. 2009a) and comparing to X-ray luminosities (Rykoff et al. 2008a,b; Rozo et al. 2009b).

In this paper, we use the X-ray luminosity-optical richness relation ($L_{\rm X} - n_{\rm gal}^{R200}$) found by Rykoff et al. (2008b) to derive the expected X-ray luminosities as

$$L_x(R_{200}) = e^{\alpha} \left(\frac{n_{\rm gal}^{R200}}{40} \right)^{\beta} \left(\frac{1+z}{1.23} \right)^{\gamma} \times 10^{42}\ h^{-2}\ {\rm erg\ s^{-1}}, \quad (1)$$

where $\alpha = 3.90 \pm 0.04$, $\beta = 1.85 \pm 0.05$ and $\gamma = 6.0 \pm 0.8$. We scale the derived X-ray luminosities to mass using a self-similar redshift evolution, in the same way as described below for the X-ray sample.

For the X-ray sample, the heterogeneity of the data makes it difficult to straightforwardly estimate the cluster masses in a uniform way. The most basic observable, available for all the sub-samples although in different bands ($[b_{\rm min}, b_{\rm max}]$), is the total cluster X-ray flux. We thus apply the scaling relation of Arnaud & Evrard (1999), linking the average gas temperature T to the bolometric X-ray luminosity $L_{\rm bol}$, with a self-similar redshift evolution to define a unique mapping between (z, $F_{\rm X}$, $b_{\rm min}$, $b_{\rm max}$) and ($L_{\rm bol}$, T). For this, we make use of the APEC spectral model (Smith et al. 2001) with heavy element abundances set to 0.3 times the solar values. The derived cluster temperatures are translated into M_{200} following the scaling law of Arnaud et al. (2005), again assuming self-similar evolution.

From simple geometric considerations and the definition of over-density with respect to the critical density, it follows that r_{200} is related to M_{200} by

$$M_{200} \equiv (4\pi/3) r_{200}^3\, 200\, \rho_{\rm c}(z), \quad (2)$$

where $\rho_{\rm c}(z)$ is the critical density of the universe at redshift z. r_{200} is typically in the range 1−3 Mpc for the clusters in our samples.

2.1.3. Cluster sample selection criteria

In order to limit our survey to massive systems, we exclude all clusters less massive than $5 \times 10^{13}\ M_\odot$ from our sample. We also exclude low-redshift systems with $z < 0.1$, in order to have the same redshift cutoff in both samples. In addition, we define a low-redshift ($0.05 < z < 0.12$) sub-sample of the X-ray sample, with the same mass cut (see Table 2), to investigate the mass dependence of the RLF (Sect. 5.3.3). The lower redshift limit of the sub-sample is chosen so as to avoid excessive overlap of low-redshift cluster fields. The upper redshift limit is chosen as high as possible without including redshifts where the mass limit of the flux-limited X-ray cluster sample is greater than our mass limit of $5 \times 10^{13}\ M_\odot$, in order to avoid a bias in the the determination of a possible mass dependence in the RLF. The fact that the low-redshift sub-sample has a slight overlap with the high-redshift X-ray sample is of little consequence as the two samples are never compared directly with one another.

Not all cluster fields in our samples are covered by the NVSS and FIRST radio surveys that are used for this study. Apart from taking this into account, we note that due to dynamic range limitations of the radio interferometric data, in the FIRST and NVSS catalogs some regions on the sky around strong radio sources are plagued by abnormally high or low source counts, often with catalog entries not corresponding to real objects[1]. We identify these regions by counting the number of sources in a circular region with radius 1° around each cluster center, and excluding fields where the source counts exceed or fall below the average counts in cluster fields by more than three standard deviations[2]. Note that using the average counts of FIRST and NVSS would slightly underestimate the expected counts in cluster fields, where a local surface over-density is expected. Counting sources within one degree of maxBCG clusters (cf. Sect. 3), we find the average density of FIRST sources in such a region to be 9% higher than the catalog average of 90 sources per square degree. In the case of NVSS, only about 4% of the cluster fields are affected by this cut (determined from the difference of rows 4 and 5 of Table 2 in the maxBCG case).

We also exclude pairs (or multiplets) of clusters where the sum of the radii (r_{200} projected on the sky plane) is greater than the angular separation between the cluster centers (row 2 of Table 2).

Table 2 summarizes the selection criteria applied to the cluster sample, and lists how many clusters in each of the final samples are covered by the FIRST and NVSS catalogs.

[1] Typical examples are the fields centered on the quasars 3C 273 and 3C 295

[2] The 1° radius corresponds to approximately ten times r_{200} at the median redshift and mass of the maxBCG sample, and is chosen so as to include all cluster sources and to have a sufficient number of background and foreground sources to allow for robust statistics.

Table 3. Properties of the FIRST and NVSS radio continuum surveys.

	FIRST	NVSS
effective resolution	5″	45″
completeness limit	1 mJy[a]	~2.5 mJy
positional uncertainty[b]	<0.5″	<1″
positional uncertainty[c]	1″	~7″
total number of sources	816 331[d]	1 810 672[3]
sources per square degree	~90	~53
area covered (deg^2)	9055	33 885

Notes. [(a)] Catalog detection threshold; [(b)] for the brightest sources; [(c)] at the completeness limit/detection threshold; [(d)] as of July 16, 2008; [(e)] as of February, 2004.

2.2. Radio source samples

2.2.1. Description of the samples

To search for radio sources associated with clusters, we use the FIRST (Becker et al. 1995; White et al. 1997) and NVSS (Condon et al. 1998) 1.4 GHz radio continuum surveys. The most relevant properties of the NVSS and FIRST surveys for the present work are summarized in Table 3. We make direct use of publicly available source catalogs from each survey. While the NVSS catalog has the advantage of greater sky coverage (cf. Table 3), thereby covering more of our cluster fields, it has the disadvantage of a poorer resolution, resulting in increased source confusion.

We search for FIRST and NVSS sources within a projected radius corresponding to 3 r_{200} around each cluster center, with r_{200} computed from Eq. (2). In order to facilitate a robust comparison of NVSS and FIRST sources, we exclude all sources fainter than 5 mJy, which is well above the completeness limit of both surveys.

In principle the use of the FIRST catalog alone would be enough for the purpose of this paper. We make use of the NVSS catalog at all stages of the analysis because it serves as a test that our results obtained with FIRST are robust. In particular, the NVSS data are important for testing our method of adaptively accounting for confusion, as described in Sect. 5.2. Because the two surveys have significant overlap, we do not need to "mix" them in the sense of combining source counts from the two catalogs for any particular sample.

2.2.2. Radio source luminosities

To compute radio luminosities, we assume isotropic emission, which is not correct for any individual galaxy, but is well justified when averaging over the entire sample. The luminosity (power) of a radio source is

$$L_{1.4\ \mathrm{GHz}} = (4\pi\, D_L^2)\, S_{1.4\ \mathrm{GHz}}\, \frac{\mathcal{K}(z)}{(1+z)}, \tag{3}$$

where $S_{1.4\ \mathrm{GHz}}$ is the angular integrated flux density taken from the VLA catalog (FIRST or NVSS), D_L is the cosmological luminosity distance and $\mathcal{K}(z)$ is the k-correction.

The radio sources are modeled with continuum spectra of the form $S_\nu \propto \nu^{-\alpha}$, where α is the spectral slope. When computing the luminosity from flux, we have to account for the fact that due to the redshift, the observed flux corresponds to a rest frequency higher than 1.4 GHz. For the computation of this so-called k-correction, $\mathcal{K}(z)$, we assign a spectral slope of $\alpha = 0.72$ to all sources, as determined by Coble et al. (2007) in the range 1.4−30 GHz. The effect of this correction is about 10% for sources at $z = 0.2$ and 30% at $z = 0.6$.

When binning the data by luminosity to compute the RLF, we determine a redshift limit, z_{cut}, for each luminosity bin to avoid counting cluster fields where the bin luminosity corresponds to a flux below our chosen threshold of 5 mJy. z_{cut} is determined from Eq. (3) and only affects the lowest luminosities considered in the analysis.

3. Radial density distribution of radio sources

As we have no redshift information for individual radio continuum sources, the over-density of sources toward clusters must be quantified statistically. We construct the stacked radial profile of radio sources around cluster centers. Following LM07, we take r/r_{200} as the radial coordinate. The resulting radial profile includes both cluster galaxies and the field (background and foreground) population. Although it cannot be decided whether individual sources are cluster members, cluster and field sources can be separated statistically, since the field population has a radially constant contribution to the radial profile. Besides determining the stacked radial density distribution of all radio sources, we also investigate whether the distribution depends on source luminosity and host galaxy cluster mass.

The radial profiles are used when constructing the luminosity function by de-projection into volume number density as described in Sect. 5.1.3.

3.1. Radial model

The angular offset of radio sources with respect to the cluster center (defined as the position of the brightest cluster galaxy (BCG) in the maxBCG sample) is translated into projected physical distance at the cluster redshift. The physical radial distances are stacked for all cluster fields and binned by radius.

We fit the radial profile of radio sources in each cluster sample by a parametric model. In general, all our radial profiles are well fit by a model of the form

$$\psi(\xi) = \psi_\beta \left(1 + \frac{\xi^2}{\zeta^2}\right)^{-\frac{3}{2}\beta+\frac{1}{2}} + \frac{1}{\xi}\psi_G e^{-(\frac{\xi}{2\sigma})^2} + \psi_{\mathrm{f}}, \tag{4}$$

where $\psi(\xi)$ is the projected surface density and $\xi = r/r_{200}$. The first term of (4) has the form of an isothermal β-model (Cavaliere & Fusco-Femiano 1978), the second term is a Gaussian, corrected for the area in an annulus, and the third term, ψ_{f}, is the constant field density.

The isothermal β-model is described by three parameters: the (peak) normalization ψ_β, the scale radius ζ, and the power law index β. The β-model is chosen because it provides a good fit to our radially binned data outside $r/r_{200} \simeq 0.006$.

In our fractional radial coordinates, the constant field density, ψ_{f}, is a function of the redshift distribution of the galaxy cluster sample. It is not physically meaningful as we have (incorrectly) placed all radio sources at the cluster redshifts, but as we are not interested in the field population this component may safely be ignored.

The second term in Eq. (4) accounts for an additional peaked feature in the radial distribution of FIRST sources in the maxBCG galaxy cluster sample (Fig. 2). It is well fit by a Gaussian with normalization ψ_{G} and variance σ^2. The origin of this feature is the fact that the cluster center is taken as the position of the BCG. As discussed further in Sect. 3.3, the underlying

Table 4. Results of β-model fits to the radial distribution of sources associated with clusters of galaxies.

Cluster sample	Source catalog	β	ζ	ψ_G	σ
maxBCG	FIRST	0.987 ± 0.018	0.0115 ± 0.0012	3.23 ± 0.18	0.00274 ± 0.00013
maxBCG	NVSS	1.018 ± 0.010	0.00257 ± 0.00019	–	–
X-ray	FIRST	0.899 ± 0.136	0.0191 ± 0.0099	–	–
X-ray	NVSS	0.911 ± 0.083	0.0198 ± 0.0063	–	–

Notes. The data are fitted using Eq. (4).

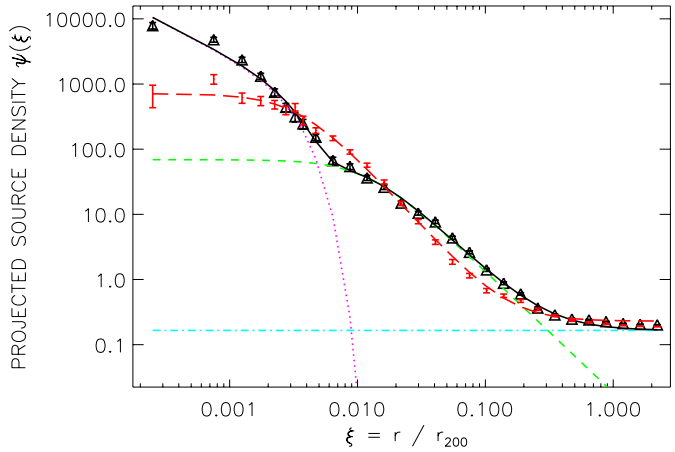

Fig. 2. Radial distribution of 1.4 GHz radio sources brighter than 5 mJy in the maxBCG cluster sample. The normalization on the y-axis is arbitrary. Radio sources selected from the FIRST catalog (triangles with error bars) clearly indicate three components: a narrow central peak, fitted with a Gaussian (dotted line); a broader distribution of sources, fitted with a β-profile (short-dashed line) and a background/foreground component (dash-dotted line). The sum of the components is indicated by the solid line. The radial profile derived from the NVSS catalog is indicated by the error bars without symbols. The fit to these data (red long-dashed line) does not include a Gaussian component.

distribution derives from the extended nature of the large majority of FIRST radio sources associated with the BCG. Note that the central Gaussian component of $\psi(\xi)$ is considered only for the radial distribution of FIRST sources in the maxBCG sample; in all other cases we set $\psi_G = 0$.

For the purpose of constructing the RLF, the exact form of the fitting function is not important; although the density profile is used in constructing the RLF (as discussed in Sect. 5.1.3), the RLF is only very weakly sensitive to the parameterization of the source density fitting function.

3.2. Dependence on luminosity and cluster mass

Because the radial distribution of sources plays an important role in determining cluster member radio source counts within r_{200}, it is necessary to investigate whether bright radio sources have a radial distribution different from the distribution of faint sources. We compute the luminosities of FIRST sources in maxBCG clusters according to Eq. (3) by placing all radio sources at the cluster redshifts and binning the sample in luminosity. We determine the radial source distribution in each luminosity bin using the fitting function given by Eq. (4). Similarly, we investigate a possible dependence on cluster mass by binning the cluster sample in mass.

Because the sample has been divided and uncertainties on individual profiles are greater, we fix the power law parameter β in Eq. (4) to the best-fit value $\beta = 0.987$ from the total fit (Table 4) in order to get reliable estimates on the scale radius ζ.

3.3. Results

3.3.1. Ensemble properties

Figure 2 shows the source density profiles in maxBCG clusters, fitted with the parametric form (4) and divided into its components. Table 4 indicates the most important parameters in the radial fits of radio sources associated with clusters.

Note that the parameters (ψ_G, σ) of the Gaussian were fit only for the FIRST sources associated with maxBCG clusters, as this is the only combination of cluster and source catalog that yields an additional centrally peaked feature. The width of the peaked distribution ($\sim 3 \times 10^{-3}\ r_{200}$) corresponds to 0.9″ at the median distance of the maxBCG clusters. Although this is comparable to the maximum positional uncertainty of FIRST point sources (~1″) at the completeness limit, the FIRST positions are typically constrained to a much better accuracy, in particular at higher flux levels. Thus, positional uncertainties in the FIRST survey alone cannot explain the width of the peaked distribution.

A visual inspection of a large fraction of ~1800 FIRST sources with positional matches out to 15″ of the maxBCG positions revealed that the very close matches (<0.3″) are dominated by compact radio sources, while the matches in the range 3″−10″ can be classified into three broad categories: (a) double sources with more or less symmetrical lobes straddling the BCG position; (b) triple sources with weak cores (centered on the BCG) and strong lobes, for which our threshold of 5 mJy picked up only the lobes; and (c) complex sources, usually of FRII or wide-angle tail type, some of which have truly spectacular radio morphologies and sizes up to 1′ or more. From this inspection we estimate that out to 10″ separation (~0.3 r_{200} at the median redshift) at least 98% of our matches correspond to the BCGs (with at most 10% of the sources being duplicates, i.e. different components or lobes of the same complex source). While for separations between 10 and 15″ (i.e. up to 54 kpc at the median redshift of the clusters of $z = 0.227$) the fraction of duplicates exceeds 30%, our matches can be safely related to the BCGs in at least 90% of the cases. We conclude that the peaked component in the radial distribution originates from mismatches in SDSS and FIRST positions caused by extended radio emission.

Because the BCG component can be separated from the general distribution of FIRST sources in the maxBCG sample, the dimensionless core radius, ζ, for the remaining sources is much larger than for the NVSS sources, where the peaked central distribution is "hidden" in the β-model component. The distribution of sources in the X-ray cluster sample is less peaked (larger ζ) because the cluster center definition is based on the gas distribution and not the position of the BCG.

We note that our results pertaining to FIRST sources in maxBCG clusters verify the radial distribution derived by

Table 5. Results of β-model fits to the radial distribution of FIRST sources associated with maxBCG clusters of galaxies, with the radio sources binned by luminosity L.

Luminosity range	ζ	σ
$\log(L\,[\mathrm{W/Hz}]) < 23.8$	0.0116 ± 0.0018	0.00249 ± 0.00067
$23.8 \le \log(L\,[\mathrm{W/Hz}]) < 24.2$	0.0138 ± 0.0023	0.00319 ± 0.00054
$24.2 \le \log(L\,[\mathrm{W/Hz}]) < 24.6$	0.0138 ± 0.0024	0.00343 ± 0.00073
$\log(L\,[\mathrm{W/Hz}]) \ge 24.6$	0.0097 ± 0.0018	0.00303 ± 0.00088

Notes. Only the parameters ζ and σ, pertaining to the width of the profiles, are listed. β has been fixed to the best-fit value 0.987 from the total fit. The data are fitted using Eq. (4).

Table 6. As table 5, but with the sample divided into mass bins.

Mass range	ζ	σ
$\log(M/M_\odot) < 13.90$	0.0132 ± 0.0016	0.00334 ± 0.00060
$13.90 \le \log(M/M_\odot) < 14.15$	0.0139 ± 0.0017	0.00344 ± 0.00075
$14.15 \le \log(M/M_\odot) < 14.40$	0.0125 ± 0.0011	0.00260 ± 0.00053
$\log(M/M_\odot) \ge 14.40$	0.0109 ± 0.0011	0.00209 ± 0.00049

Croft et al. (2007) for the same sample. As indicated in Fig. 2, our narrow binning reveals the details of the centrally peaked component in detail and confirm its origin as the BCG population. The relatively high redshifts in the optical sample ($z \ge 0.1$) also imply that the population of star forming galaxies in clusters – with a broader distribution than radio-loud AGN – has been excluded by our flux limit of 5 mJy. As a consequence our β-model fit to the radial profile is much narrower compared to those obtained for the radio source distribution in nearby galaxy clusters (e.g. Reddy & Yun 2004; Massardi & De Zotti 2004). Similar narrow radial profiles consisting mostly of radio-loud AGN were also found by LM07.

3.3.2. Luminosity and cluster mass dependence

From their X-ray sample of galaxy clusters, LM07 found that more luminous radio sources are more centrally concentrated in galaxy clusters. As indicated in Table 5, we are unable to reproduce this result with our optical maxBCG sample; although the highest luminosity bin has a slightly smaller scale radius ζ of the outer profile, the result is not significant. Similarly, there is no statistically significant indication of a mass dependence of the radial density from the maxBCG sample of galaxy clusters (Table 6). We verify that the same is the case when using the NVSS sample.

4. Mass-luminosity correlation

In this section we investigate the correlation between cluster mass and the radio luminosity of the brightest radio source in the central region of the cluster. We compare the results with similar studies done with the optical luminosities of the brightest cluster galaxies, and discuss the implications for our goal of comparing the volume averaged radio luminosity function in clusters at different redshifts.

4.1. Background

Brightest cluster galaxies (BCGs) tend to lie at the center of the mass distribution and are more luminous than average ellipticals. Moreover, their properties correlate strongly with their host clusters, as seen from numerical simulations (e.g. De Lucia & Blaizot 2007) and optical/near-IR observations (e.g. Lin & Mohr 2004; Brough et al. 2008). It has been shown that BCGs are about an order of magnitude more likely than other ellipticals to host radio-loud AGN (Edge 1991; Lin & Mohr 2004; Best et al. 2007). Based on this, it is likely that the most radio-luminous galaxies in clusters are associated with BCGs, and in addition to the correlation between BCG luminosity and cluster mass one can expect that 1.4 GHz radio luminosities of the central radio-loud AGN are also correlated with cluster mass.

4.2. Method

We investigate the correlation of BCG radio luminosity with cluster mass by taking the luminosity of the single brightest source within a radius of 50 kpc from the cluster center. We reiterate that the latter is actually the BCG position in the maxBCG sample. In the X-ray sample, the search radius allows for offsets between the X-ray center and the BCG position; Koester et al. (2007) found typical offsets of 50 h^{-1} kpc by cross-correlating the maxBCG catalog with NORAS and REFLEX data.

Note that this selection method leads to a different minimum flux level for different redshift sub-samples, since we are disregarding clusters that do not contain any radio source above a certain flux density. This leads to a higher mean luminosity of the central radio source for clusters at higher redshift, compared to clusters at lower redshifts within the same mass bin (derived from the X-ray or optical mass observables). The actual redshift evolution of the radio luminosities of the central BCGs is hidden within this luminosity bias. Considering the large scatter in the luminosity of the central radio source, we do not attempt to model the redshift evolution from this method.

4.3. Results

Figure 3 shows the correlation of luminosities of FIRST sources with cluster mass for both our cluster samples. Modeling the correlation with a power-law of the form $L \sim M^\alpha$, the best-fit correlation from the maxBCG sample in the redshift range $0.1 < z \le 0.2$ is $\alpha = 0.31 \pm 0.12$. Although the X-ray sub-sample in the same redshift range is essentially too small to constrain the power law, the data are consistent with the maxBCG result, with $\alpha = 0.34 \pm 0.41$. The low-redshift X-ray sub-sample yields $\alpha = 0.44 \pm 0.27$, again consistent with the maxBCG relation.

The found correlation between radio luminosity and cluster mass is consistent with results from optical/near-IR observations of the BCGs. Lin & Mohr (2004) compared the K-band near-IR luminosities for a sample of X-ray selected clusters and found $L_{\mathrm{BCG}} \propto M_{\mathrm{cl}}^{0.26\pm0.04}$. Haarsma et al. (2010) reported a shallower correlation from an X-ray selected sample; $L_{\mathrm{BCG}} \propto M_{\mathrm{cl}}^{0.18\pm0.07}$. Thus, luminosities in other bands show correlations with mass that are similar to our results.

For the optical cluster sample, the correlation of radio luminosity and cluster mass strongly points towards increased radio emission from the central AGN in the BCGs of more massive clusters. Croft et al. (2007) also computed the rest-frame 1.4 GHz luminosities of the BCGs by cross-correlating the maxBCG catalog with the FIRST survey, and noted the trend of increasing radio luminosity with optical luminosity of the BCGs in the r-band. We do not expand on this result further, as the radio luminosity of the central brightest radio source is a poor indicator of the total radio luminosity in clusters. A cluster can have

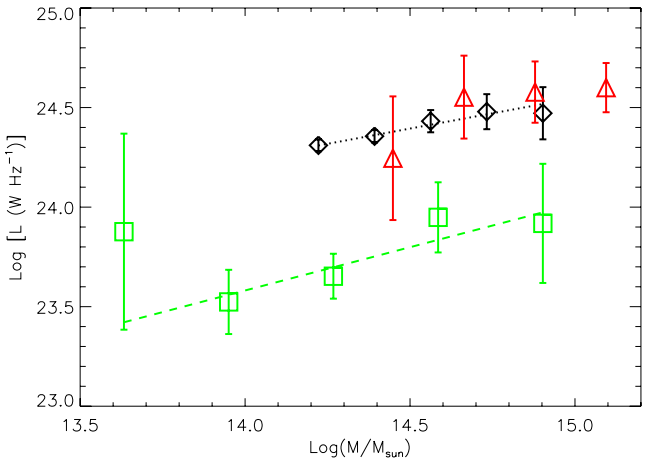

Fig. 3. Correlation between radio luminosity of the brightest FIRST source within a projected physical radius of 50 kpc from the cluster center (BCG position in the maxBCG sample) and cluster mass for three sub-samples of galaxy clusters. Diamonds indicate maxBCG clusters in the redshift range $0.1 < z \leq 0.2$, and the best-fit correlation is indicated by the dotted line. This is consistent with the X-ray sample in the same redshift range (triangles). Fixing the slope, the correlation is consistent with a local sub-sample of X-ray clusters ($0.01 < z \leq 0.1$, squares), where the luminosity level is lower due to a different luminosity cutoff in this sub-sample.

multiple BCGs as a result of its merging history[4], and the radial source density profile in Fig. 2 suggests that the radio source population extends beyond the cluster core region. For these reasons, we now turn to the construction and modeling of the volume averaged radio luminosity function in galaxy clusters.

5. The radio luminosity function

In this section, the radio luminosity function (RLF) is derived for each of our samples. We start by discussing how accurate source counts in the cluster volume are obtained (Sect. 5.1). In Sect. 5.2 we describe how source confusion is accounted for. We describe a parametric model for the RLF in Sect. 5.3, and also discuss how a redshift evolution is modeled. We give the results in Sect. 5.4. We discuss systematic uncertainties in Sect. 5.5, and compare our results to previous work in Sect. 5.6.

5.1. Method

The luminosity function $\phi(L)$ is defined as the average number of radio sources per unit physical volume of a cluster and per logarithmic luminosity bin ("magnitude"). We use the estimated values of r_{200} from Sect. 2.1 to define cluster volumes, expressed in Mpc^3.

5.1.1. Source counts

Figure 4 illustrates schematically how source counts are obtained. For each cluster, a region within a projected physical radius $r = \eta\, r_{200}$, from the center is searched for radio sources in a given luminosity bin, using the cluster redshift to convert from flux to luminosity. As explained below, the search radius does not have a systematic effect on the RLF; however, it can

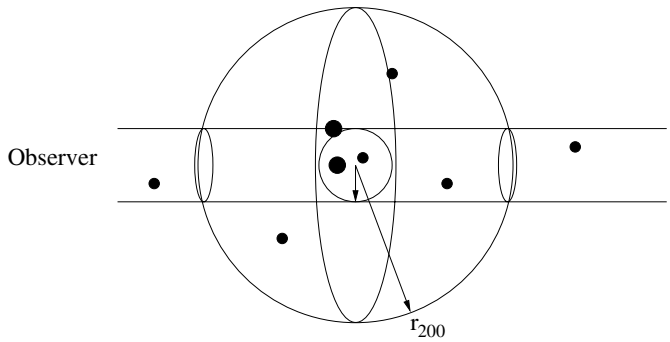

Fig. 4. Illustration of the method used to obtain source counts and volumes for the computation of the luminosity function of radio sources inside clusters. For each cluster the sampled volume is the "line-of-sight cylinder". The projected number density in this volume is converted to volume density of sources inside the cluster radius (r_{200}) by applying a model for the volume density of sources.

be chosen such as to minimize the uncertainties of the latter. The number of sources found within the chosen radius is $N_\eta^{\rm count}$. We need to convert this number into a de-projected number of sources within r_{200}. For this, we need to know (i) the number of foreground/background sources; and (ii) the radial source density profile. In the following we discuss these issues in turn.

5.1.2. Field subtraction

To correctly model the field counts, we first need to understand the mean surface number density of radio sources in the sky as a function of flux. For this we bin the FIRST and NVSS catalogs in their entirety in logarithmic flux bins to derive an estimate of the number of sources per flux interval and solid angle, $\frac{{\rm d}N}{{\rm d}S\ {\rm d}\Omega}$. Due to the large sample size of both NVSS and FIRST, this quantity is well constrained except at very low and very high flux densities. Because it is difficult to find a generally valid fitting function, we model $\frac{{\rm d}N}{{\rm d}S\ {\rm d}\Omega}$ using quadratic spline interpolation between bins.

The number of foreground/background sources, $N_\eta^{\rm field}$, inside the search radius of a given cluster is determined by integrating over the field density[5] as

$$N_\eta^{\rm field} = \Omega \int_{S_{\rm min}}^{S_{\rm max}} \frac{{\rm d}N}{{\rm d}S\ {\rm d}\Omega} {\rm d}S, \qquad (5)$$

where Ω is the angular area of the searched region, and $S_{\rm min}$ and $S_{\rm max}$ are determined from the limiting values of the luminosity bin according to Eq. (3).

The total number of cluster sources inside the search radius is

$$N_\eta = N_\eta^{\rm count} - N_\eta^{\rm field}.$$

Uncertainties on N_η are computed from Poisson statistics as discussed by Gehrels (1986).

For reasons of simplicity, the previous discussion has focused on source counts in a single cluster field. However, it is straightforward to apply the method discussed here to the entire stack of clusters by adding all individual N_η.

5.1.3. De-projection into cluster volume

To convert the cluster source counts N_η inside the "line-of-sight cylinder" (cf. Fig. 4) limited by $\eta\, r_{200}$ to counts N inside r_{200},

[4] After a cluster merger, it will take considerable time before the two initial BCGs cease to dominate their subgroups and one of them comes to dominate the merged cluster

[5] We approximate the *field* as the sum of all regions on the sky covered by the radio survey, minus circular regions around the sample clusters, defined by the respective radii (r_{200}) estimated from scaling relations.

we compute the expected ratio of sources inside the sphere delimited by r_{200} and inside the cylinder. We integrate the spatial source density, as a function of de-projected radius, over the two regions and take the ratio

$$C_N(\eta) = \frac{N_{\rm sphere}}{N_{\rm cylinder}} = \frac{4\pi \int_{\Xi=0}^{1} \Psi(\Xi)\,\Xi^2\,{\rm d}\Xi}{2\pi \int_{z=-\infty}^{+\infty} \int_{\rho=0}^{\eta} \Psi\left(\sqrt{\rho^2+z^2}\right)\rho\,{\rm d}\rho{\rm d}z}, \quad (6)$$

where $\Psi(\Xi)$ is the de-projected counterpart of $\psi(\xi)$ (cf. Eq. 4). Note that $\Xi = r/r_{200}$, with r now being the de-projected (physical) coordinate. The integral over the line-of-sight cylinder (in the denominator) is written in cylindrical polar coordinates, with $\sqrt{\rho^2+z^2} = \Xi$.

The de-projected source distribution $\Psi(\Xi)$ is derived from the projected source density distribution $\psi(\xi)$, discussed in Sect. 3. Because no dependence on luminosity could be determined for $\psi(\xi)$, we use the parameters derived from the total sample for each combination of cluster and radio source catalogs, as listed in Table 4.

Because the central Gaussian component of $\psi(\xi)$ in Eq. (4) does not correspond to a physical distribution of sources (cf. Sect. 3), it is not physically meaningful to de-project it to physical coordinates. However, because the component is narrow, we can make the approximation that all sources belonging to it (i.e. all BCGs) have been counted inside the line-of-sight cylinder, provided η is chosen large enough ($\eta \gtrsim 0.1$). Thus, no correction in the sense of Eq. (6) is required for the central component.

We compute a correction factor only for the broader β-model. In order to avoid over-correction where the narrow component is present, we compute from (4) the relative fraction of sources belonging to the broader profile and multiply the correction factor by this number to yield a modified correction factor, $\tilde{C}_N$.

For the isothermal β-model, the physical (de-projected) density of the sources is given by (e.g. Sarazin 1988)

$$\Psi(\Xi) = \Psi_\beta \left(1 + \frac{\Xi^2}{\zeta^2}\right)^{-\frac{3}{2}\beta}, \quad (7)$$

which is the function we use when computing the integrals in Eq. (6). The parameters (β, ζ) are unique for each galaxy cluster sample, as discussed in Sect. 3. Because we are only interested in ratios, we set $\Psi_\beta = 1$.

The cluster volume is defined as a sphere with radius r_{200}. Thus, the RLF in luminosity bin ΔL can be expressed as

$$\phi(L)\Delta L = \tilde{C}_N \frac{N_\eta}{V_{\rm sph}}, \quad (8)$$

where $V_{\rm sph}$ is the sum of physical cluster volumes (within r_{200}), and N_η is the total number of sources (in all cluster fields) found within a radius $\eta\, r_{200}$ and having luminosities in the luminosity bin ΔL.

The uncertainty in the RLF is dominated by Poissonian noise in the source counts. We compute the uncertainty by scaling from the uncertainty δN_η in N_η as

$$\frac{\delta(\phi(L)\Delta L)}{\phi(L)\Delta L} = \frac{\delta N_\eta}{N_\eta}.$$

By construction, the RLF is insensitive to the chosen value of the projected fractional radius η after the correction factor $\tilde{C}_N$ has been applied. However, uncertainties in the RLF can be minimized by carefully tuning this parameter. Values too close to 1 will increase the background counts, and thereby the error, since there are few cluster sources close to r_{200}. On the other hand, too low values of η will increase uncertainties due to not providing enough cluster sources for good statistics. We find that $\eta = 0.5$ provides a good balance between cluster and background sources, and use this value in computing the RLF.

5.2. Confusion

Confusion becomes important when the typical separation of sources is comparable to the angular resolution of the radio survey from which the RLF is derived. In particular, a larger beam tends to overestimate the RLF at the high luminosity end as several confused low luminosity sources appear as fewer sources with higher luminosity. This effect is redshift dependent through the conversion of angular to physical distance, which complicates quantifying a possible redshift evolution in the RLF.

Comparing the narrow radial distribution of sources (Sect. 3) with the resolution of the FIRST survey, it is apparent that confusion affects the counts also when using FIRST data. This will affect the shape and normalization of the RLF in a way that we have no direct way of quantifying. However, our main interest is to constrain the redshift evolution of the RLF, and for this purpose the absolute normalization of the RLF is of less importance. Therefore, rather than attempting to correct for confusion, we can correct for the relative difference in confusion at different redshifts.

5.2.1. Degrading the resolution of the radio data

To address the confusion problem, we thus degrade the resolution of the radio source data in an adaptive way to make sure that confusion effects are the same at all redshifts (disregarding second order effects such as a number density evolution in the central parts of clusters influencing the confusion problem). In the following, we discuss how the resolution of the radio source data can be degraded. To demonstrate the method, we apply it to the FIRST catalog to enable a direct comparison of the RLF derived from FIRST to that derived from NVSS, before discussing how the method is used in removing first-order systematic effects of confusion in the redshift evolution of the RLF.

The full-width half maxima (FWHM) of the FIRST and NVSS synthesized beams are 5″ and 45″, respectively. To what extent individual sources can be distinguished in each of the surveys, however, largely depends on their absolute and relative brightnesses. Here we make the simplification that given a resolution in terms of a beam FWHM, no two sources are resolved if their mutual separation (irrespective of flux) is less than the FWHM.

To degrade the resolution of the FIRST or NVSS data, we define a beam with a FWHM larger than that of the original data. In a given field, the position and flux density of each source are recorded. The brightest source is located, and all sources within a radius equal to the FWHM around this source are combined into one source. The position of the new source is taken as a flux-weighted average of its parts, and the total flux density is the sum of the integrated flux densities of the parts. The next brightest source (excluding all sources that have already been considered) is then located, and the procedure is repeated until no two sources are separated by an angular distance less than the FWHM. Note that this method is limited by the use of source

catalogs in the sense that sources fainter than a chosen limit will not be considered. Here we use the completeness limit of the two source catalogs to determine which sources to consider for summing.

As an improved method, one could instead use the raw maps of cluster fields from the FIRST survey and degrade them to the NVSS resolution before extracting sources. However, this requires a robust source extraction in both maps and is quite complicated for faint sources near the completeness limit of the surveys. Moreover, neither such a method nor the method described above can resolve the inherent problem that some extended emission recovered by NVSS is resolved out by FIRST.

5.2.2. NVSS and FIRST source counts

A simple way to visualize the effect of confusion on the RLF is to compare the luminosity function as constructed from NVSS with that constructed from FIRST, using the same completeness cutoff in both surveys. For this comparison we select cluster fields in a narrow redshift range, $0.1 \leq z \leq 0.16$, from the maxBCG catalog to ensure a sufficiently large statistical sample. This sub-sample of the maxBCG catalog is used only for the purpose of directly comparing luminosity functions constructed from FIRST and NVSS in this section. It contains 2341 clusters with $M_{200} > 5 \times 10^{13}\ M_{\odot}$ which are covered by NVSS and FIRST. As indicated in Fig. 5, computing the RLF directly from the two radio source samples yields inconsistent results. This is expected due to confusion effects.

We attempt to re-create the NVSS based luminosity function from the FIRST data by degrading the resolution as described above. Note that we do not expect a perfect agreement since the sensitivity to spatial frequencies of FIRST is very different from that of NVSS.

Because both surveys have many sources separated by distances much smaller than the respective resolutions (due to the specific source extraction methods applied to the synthesized images), we impose a strict lower limit of 45″ on the separation of sources in *both* surveys for this comparison. The results are shown in Fig. 5. Even using this simple method, the RLF from the degraded FIRST sample is in good agreement with that derived from the NVSS counts. The RLF constructed from the degraded FIRST data is systematically lower than that constructed from the degraded NVSS data. This is as expected considering the different sensitivities to spatial frequencies of the two surveys – extended emission recovered by NVSS is resolved out by FIRST, causing the amplitude of the RLF to drop. Note, however, that the difference in the luminosity function at different redshifts caused by this effect will in fact be much smaller than the residual difference seen in Fig. 5, since our relatively small redshift range in the maxBCG sample results in a much smaller relative difference in physical scales, as compared to the relative difference between the FIRST and NVSS synthesized beams.

5.2.3. Accounting for confusion

Given the above model, it is possible to adaptively introduce confusion into our radio source sample to minimize systematic effects in determining the redshift dependence of the RLF. In a given cluster sample, the clusters with the greatest angular diameter distances will be the most affected by confusion. Thus, we define a nominal "confusion distance", in physical units, by converting the radio source survey resolution (45″ for NVSS or 5″ for FIRST) to a physical distance at the redshift of the object with the greatest angular diameter distance in the sample. Then, for every object in the sample, this physical distance is converted back to angular units using the redshift of the object, and the resulting angular scale is used to degrade the resolution of this particular cluster field using the method described above.

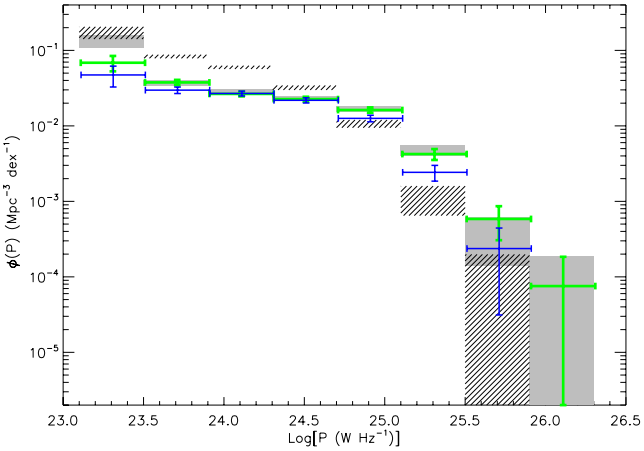

Fig. 5. Change in the RLF resulting from degrading the resolution of both the FIRST and NVSS catalogs to a minimum source separation of 45″ (the FWHM of the synthesized beam of NVSS). The shaded regions indicate the RLF computed from the non-degraded NVSS (grey) and FIRST (hashed) data. The error bars indicate the degraded versions; here the counts derived from the FIRST catalog (blue, thin error bars) are in approximate agreement with the NVSS counts (green, thick error bars), despite the large difference in synthesized beam FWHM of the original data.

To get an idea of the typical level of confusion, consider the maximum redshift, $z = 0.3$, of the maxBCG catalog. The FIRST resolution of 5″ corresponds to a physical distance of 22 kpc at this redshift. We can translate this physical distance, the "confusion distance", into an angular distance at any lower redshift; for example, at the low redshift limit of $z = 0.1$ we obtain an angular scale of 12″. Using this as a limit of resolution, the FIRST source counts are reduced by approximately 25% in fields defined by r_{200}, while at $z = 0.3$ the FIRST source counts are reduced by around 10%[6].

Note that we also have to adapt the background counts, $N_{\eta}^{\mathrm{field}}$, when degrading the resolution. Because it is time consuming to re-compute $\frac{\mathrm{d}N}{\mathrm{d}S\,\mathrm{d}\Omega}$ for each angular resolution used, we compute the field counts in several degraded versions (as described in Sect. 5.2.1) of the entire NVSS and FIRST catalogs, using increments of 5″, and interpolate between these results to derive estimates of $N_{\eta}^{\mathrm{field}}$ individually for all cluster fields.

5.3. Modeling the luminosity function

5.3.1. Parametric model

To allow for a quantitative estimate of the redshift evolution of the RLF, we follow LM07 and use the parameterization

$$\log \phi = y - \left(b^2 + \left(\frac{\log L - x}{w} \right)^2 \right)^{1/2} - 1.5 \log L. \qquad (9)$$

This fitting function was used by Condon et al. (2002) to fit the field RLF using the combined contributions from radio-loud

[6] The counts are reduced also at the resolution limit because, contrary to the FIRST catalog, we enforce a strict limit of 5″ as the smallest angular distance between two distinct sources.

AGN and star-forming (SF) galaxies. LM07 used the two sets of values of (b, x, w) found by Condon et al. to make possible a separation of the normalizations (y) of the radio-loud AGN and SF components in their cluster RLF at low redshift.

It is beyond the scope of this paper to discuss the physical interpretation of Eq. (9) as our main concern is the redshift evolution of the luminosity and number density. Refer to Condon et al. (2002) and references therein for details on this hyperbolic fitting form of the RLF.

In contrast to the sample studied by LM07, our main samples do not include systems with $z < 0.1$. This selection, combined with our flux limit of 5 mJy, effectively ensures that we are only sensitive to the high-luminosity radio-loud AGN population of the RLF. Thus, a one-component model as described by Eq. (9) is sufficient for the present purpose.

5.3.2. Redshift evolution

Machalski & Godlowski (2000) quantified the redshift evolution of the RLF under the assumption that the overall shape remains constant, as first suggested by Condon (1984). Under this assumption, there can only be changes in overall luminosity and overall number density. The redshift dependence can be written as

$$\phi(L, z) \;=\; g(z)\, \phi\left[Lf(z), z \approx 0\right], \tag{10}$$

where $g(z)$ quantifies the number density evolution, corresponding to a vertical shift ΔY in $\phi(L)$, and $f(z)$ represents luminosity evolution, corresponding to a horizontal shift ΔX:

$$\log\left[\phi(\log L, z)\right] \;=\; \log\left[\phi(\log L + \Delta X, z \approx 0)\right] \;+\; \Delta Y. \tag{11}$$

The vertical and horizontal shifts can be fitted to yield $f(z)$ and $g(z)$. Shape preservation of the RLF in $(\log L, \log \phi)$ space implies that number density and luminosity scale as powers of redshift. For the luminosity,

$$L = L_0 \left(\frac{1+z}{1+z_0}\right)^{\alpha_{\rm L}}, \tag{12}$$

where $\alpha_{\rm L}$ is the power law index, and correspondingly for the number density

$$\phi = \phi_0 \left(\frac{1+z}{1+z_0}\right)^{\alpha_\phi}, \tag{13}$$

with the power law index α_ϕ.

To constrain the redshift evolution in the RLF, we bin our samples by redshift, and approximate the redshift in each bin by the median of all cluster redshifts in the bin. We then apply (9), shifted in ϕ and L according to (11), to constrain the power law indices α_ϕ and $\alpha_{\rm L}$. Simultaneously, the four parameters of (9) are constrained.

We let the parameter y in (9) represent the normalization of the RLF at $z = 0$. We bin the data by redshift and construct the RLF separately for each redshift bin. The thus constructed luminosity function data are then used simultaneously to constrain y, b, x, w, α_ϕ and $\alpha_{\rm L}$. The fitting is carried out by minimization of the χ^2 statistic,

$$\chi^2 = \sum_{i=1}^{k} \left(\frac{X_i - \mu_i}{\sigma_i}\right)^2, \tag{14}$$

where X_i is the data point with index i (the number k of data points is the total number of luminosity bins in all redshift bins), μ_i is the corresponding model value given a set of parameters (y, b, x, w, α_ϕ and $\alpha_{\rm L}$), and σ_i is the uncertainty on data point i estimated from Poisson statistics.

Uncertainties on the fitted parameters are estimated using a simple method. Given our data points, binned in redshift and in luminosity, we vary the data according to Poisson statistics within their estimated uncertainties, and carry out the χ^2 fit again. This process is repeated 10.000 times. As expected, the mean of the distribution of a fitted parameter in any of the fits we carry out (Sect. 5.4.2) corresponds to its best-fit value. The standard deviation of the distribution of a fitted parameter is used as an estimate of the 1σ uncertainty of this parameter.

5.3.3. Mass dependence

A possible mass dependence in the RLF can be investigated using the same method as described above. By scaling the number density and luminosity we can model the dependence to a first approximation as power laws of the form M_{200}^{γ}. Analogously with the discussion in Sect. 5.3.2, we make the assumption of shape preservation of the RLF and model the luminosity and number density dependence on mass as (cf. Eqs. (12) and (13))

$$\begin{aligned} L &\sim (M_{200})^{\gamma_{\rm L}}; \\ \phi &\sim (M_{200})^{\gamma_\phi}. \end{aligned} \tag{15}$$

We use both the X-ray sample and the optical sample to constrain the mass dependence. Because two new parameters are introduced into the model, it is not possible to simultaneously constrain the mass dependence and the redshift evolution, particularly given the limited size of the X-ray sample. For this reason we use a sub-sample of the X-ray selected clusters in a low redshift range of $0.05 \le z \le 0.12$ (see Table 2). In this range, we divide the sample into two mass bins, where care is taken that the lower mass limit of the lower mass bin is above the completeness limit of the X-ray sample at $z = 0.12$. For the optical sample, we divide the complete sample into three mass bins. In the next section it is shown that in this range, our data are consistent with no mass dependence of the RLF.

5.4. Results

5.4.1. Mass dependence

To separate a possible mass dependence in the RLF from a pure redshift dependence, we construct RLF binned by mass as shown in Figs. 6 and 7. We then use a least-squares statistic to find the best-fit vertical and horizontal shifts of the RLF, fixing the values of b, w, x as described in Sect. 5.3.2, to interpret the shifts in terms of a luminosity- and/or number density dependence on cluster mass. The results for both our cluster catalogs are given in Table 7, using different priors on the power laws. Note that all fits are consistent with $\gamma_\phi = 0$ and $\gamma_{\rm L} = 0$ at an approximate 1σ level.

Thus, contrary to LM07, who find that the amplitude of the RLF for low-mass clusters is slightly larger at the low-luminosity end, we find no evidence of a mass dependence in the RLF given our flux and redshift cut-offs. As indicated in Fig. 6, the results are consistent with the most luminous radio sources only being found in high-mass clusters, as was also found by LM07. However, due to the relatively small sample size, our data provides no conclusive evidence of this.

As there is no statistically significant indication of a mass dependence from either cluster sample, we proceed to fit for a pure redshift evolution in the next subsection.

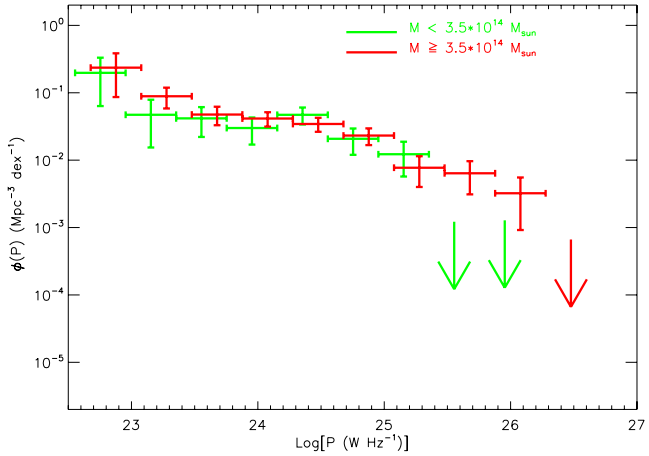

Fig. 6. RLF determined from the X-ray subsample in the redshift range $0.05 \leq z \leq 0.12$, divided into two mass bins. Arrows indicate 1σ upper limits from Poisson statistics.

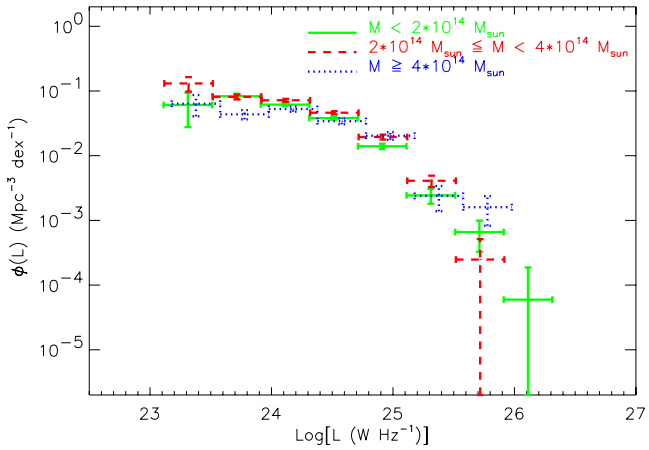

Fig. 7. RLF determined from the optical sample, divided into three mass bins.

Table 7. Mass dependence of the RLF, parameterized in terms of power laws of M_{200} in luminosity and number density (Eq. (15)).

Cluster sample	Source catalog	Prior	γ_ϕ	γ_L
X-ray	FIRST		0.25 ± 1.01	–0.46 ± 0.55
maxBCG	FIRST		–0.36 ± 0.31	0.38 ± 0.65
X-ray	FIRST	$\gamma_\phi = 0$	(0.0)	0.13 ± 0.36
maxBCG	FIRST	$\gamma_\phi = 0$	(0.0)	0.27 ± 0.28
X-ray	FIRST	$\gamma_L = 0$	0.090 ± 0.16	(0.0)
maxBCG	FIRST	$\gamma_L = 0$	0.046 ± 0.15	(0.0)

5.4.2. Redshift evolution

Figure 8 shows the RLF computed from the maxBCG sample, using FIRST radio sources, in three redshift bins chosen such that there are approximately the same numbers of clusters in each bin ($0.1 \leq z < 0.17$, $0.17 \leq z < 0.24$ and $0.24 \leq z \leq 0.3$). We apply the method outlined in Sect. 5.3.2 to constrain the redshift evolution of the RLF by a simultaneous fit to the RLF amplitude (parameterized by y at $z = 0$), the RLF shape (parameterized by b, x and w), and the power law evolution (parameterized by α_ϕ and α_L according to Eqs. (12) and (13)).

We perform a number of fits to the data, with priors as listed in Table 8. Although a simultaneous fit to both α_ϕ and α_L yields

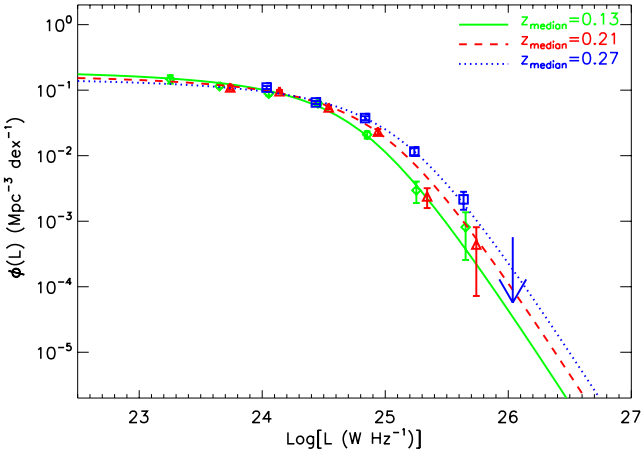

Fig. 8. Redshift evolution in the RLF determined from the optical (maxBCG) sample, without priors. The data are shown as error bars and the best simultaneous fit to luminosity and number count evolution is represented by lines corresponding to the redshift bins: $0.1 \leq z < 0.17$ (diamonds and solid line), $0.17 \leq z < 0.24$ (triangles and dashed line), and $0.24 \leq z \leq 0.3$ (squares and dotted line).

the best fit (in the sense of the reduced χ^2 parameter, $\chi^2_{\rm red}$, being the closest to unity), the data are consistent with no number density evolution. Note that the best-fit value $\alpha_\phi = -1.38$ implies *fewer* radio-loud AGN at higher redshift within the range $0.1 \leq z \leq 0.3$. Though not unphysical, such a negative evolution is unlikely, considering the evidence of increased AGN activity in the field population (Dunlop & Peacock 1990), and the enhanced AGN fraction within clusters as seen from X-ray observations (Eastman et al. 2007; Galametz et al. 2009) Therefore, we carry out an additional fit in which we fix the number density power law to zero and fit for a pure luminosity evolution. The result is a positive luminosity evolution with $\alpha_L = 3.99 \pm 1.24$. While consistent with a pure luminosity evolution, the data are inconsistent with a pure number density evolution, as indicated by the $\chi^2_{\rm red}$ of the third column in Table 8.

The last three rows of Table 8 indicate the results of fitting the evolution parameters to the X-ray derived RLF, also binned by redshift (redshift bins: $0.1 \leq z < 0.2$, $0.2 \leq z < 0.45$ and $z \geq 0.45$). Although the X-ray sample extends to greater redshifts than the maxBCG sample, it has less leverage on the redshift evolution because of its limited size. For this reason, we fit only for y, α_ϕ and α_L. We keep the shape parameters fixed to the values found in the maxBCG/FIRST fit, as this is the fit with the smallest uncertainties. Because the smallest $\chi^2_{\rm red}$ is measured for the case of no priors (as expected) in the maxBCG/FIRST case, we use the results of this fit for fixing the shape parameters. Again, we also carry out fits to pure luminosity evolution and pure number density evolution. At one standard deviation, the results from the X-ray sample are consistent with those of the optical maxBCG sample. Again, a pure number density evolution provides a poor fit to the data.

We note that in all cases the fit is especially sensitive to the parameter b, which is explained by its quadratic dependence in Eq. (9).

5.5. Systematic uncertainties

To estimate systematic uncertainties in the luminosity and number density evolution of the RLF, we discuss below four separate sources of error.

Table 8. Redshift evolution in the RLF, quantified by simultaneous fits to the RLF amplitude, shape and evolution.

Cluster sample	Source catalog	Priors	y	b	x	w	α_ϕ	α_L	χ^2_{red}
maxBCG	FIRST		36.38 ± 1.02	1.05 ± 0.73	24.53 ± 0.18	0.66 ± 0.13	−2.46 ± 1.58	6.20 ± 1.76	1.07
maxBCG	FIRST	$\alpha_\phi = 0$	36.34 ± 0.92	0.91 ± 0.81	24.87 ± 0.14	0.72 ± 0.21	(0.0)	3.99 ± 1.24	1.19
maxBCG	FIRST	$\alpha_L = 0$	36.74 ± 0.89	1.01 ± 0.55	25.11 ± 0.11	0.71 ± 0.19	1.03 ± 1.14	(0.0)	2.25
X-ray	FIRST	(a)	36.19 ± 0.19	(1.05)	(24.53)	(0.66)	0.76 ± 1.86	8.12 ± 2.67	0.94
X-ray	FIRST	(a); $\alpha_\phi = 0$	36.26 ± 0.10	(1.05)	(24.53)	(0.66)	(0.0)	8.19 ± 2.66	0.89
X-ray	FIRST	(a); $\alpha_L = 0$	35.89 ± 0.18	(1.05)	(24.53)	(0.66)	9.40 ± 1.85	(0.0)	10.48

Notes. The goodness-of-fit is indicated by the reduced chi-squared parameter, χ^2_{red}. See Sect. 5.3 for a description of the parameters.
[(a)] The shape parameters b, x and w were fixed to the results of the maxBCG/FIRST analysis with no priors.

Table 9. Summary of systematic effects on the number density and luminosity evolution of the RLF.

Systematic	Effect on α_ϕ	Effect on α_L
$L_{bol} - T$ scaling	±0.30	
$L_X - n_{gal}^{R200}$ scaling[a]	±0.80	
k-correction	$^{+0.15}_{-0.51}$	$^{+0.17}_{-0.16}$
Totals[b]		
maxBCG	$^{+0.87}_{-1.00}$	$^{+0.17}_{-0.16}$
X-ray	$^{+0.33}_{-0.59}$	$^{+0.17}_{-0.16}$

Notes. [(a)] Only for maxBCG clusters; [(b)] added in quadrature.

The estimated systematic uncertainties for the maxBCG and X-ray samples are summarized in Table 9. For each uncertainty estimate, we keep all parameters but the RLF normalization and the evolution parameter in question (α_ϕ or α_L) fixed, while carrying out the complete RLF analysis with posterior assumptions altered as described above. To estimate total systematic effects on α_ϕ and α_L, we add all relevant components in quadrature. We note that for this study, the statistical errors on the fitted parameters (see Table 8) still dominate over the systematics.

5.5.1. Scaling relations

Uncertainties in the z-dependence of the scaling relations used to derive cluster masses affects the derived number density evolution through the indirect determination of cluster volumes. For the X-ray sample, we estimate this systematic by replacing the self-similar evolution of the $L_{bol} - T$ relation by (i) the strong evolution measured by Kotov & Vikhlinin (2005) and (ii) by assuming no evolution of the $L_{bol} - T$ relation. Re-computing the M_{200} for both cases results in a change in the number density evolution parameter α_ϕ of ±0.30 when re-computing the RLF for the X-ray sample. For the optical sample, we additionally need to take the uncertainty in the $L_X - n_{gal}^{R200}$ relation (Eq. (1)) into account. We estimate the systematic effects by using the extreme values (at 1σ confidence) of the redshift dependence from Rykoff et al. (2008b) to re-compute M_{200}, resulting in an effect on α_ϕ of ±0.80.

5.5.2. k-correction

Uncertainties in the k-correction used in converting from radio source flux to luminosity will mainly affect the luminosity evolution. It can also shift the number density evolution by assigning the wrong luminosity bins to sources.

As extreme values of the ensemble average spectral slope, we use the 25th and 75th percentiles ($\alpha = 0.51$ and $\alpha = 0.92$, respectively) of the slope distribution of Coble et al. (2007). We recompute the maxBCG RLF using these extreme spectral slopes for all sources.

5.5.3. Source counts

Incorrect radio source counts can be caused either by counting extended or complex sources (e.g. AGN with radio lobes) as several separate sources, or by not resolving unrelated sources. This affects the number density and luminosity evolution only if the effect is varying with redshift; otherwise a mere offset in the normalization of the RLF is introduced.

A complete treatment of these effects would require the careful visual inspection of the radio maps in each cluster field, which is not feasible for a large sample such as maxBCG. Instead we carried out a visual inspection on parts of the sample to estimate the possible effects. We visually inspected FIRST maps in the 500 fields corresponding to the clusters with the lowest redshifts, and in the 500 fields corresponding to the clusters with the highest redshifts of the maxBCG sample, taking weighted sums of the flux densities of FIRST catalog entries deemed to be different components or lobes of the same sources. Ambiguous cases (less than 2% of the fields studied) were removed. Comparing the RLFs constructed from the modified FIRST data in the two sub-samples, we noted a drop in normalization of the RLF by about 5% in both the high-z and the low-z subsamples. There was no indication of a significant change to the evolution of the RLF within our statistical errors. Thus, we conclude that our adaptive accounting of confusion with redshift (Sect. 5.2) is sufficient to deal with this systematic, at least for the purpose of constraining the redshift evolution of the RLF.

5.5.4. Radio source flux

Systematic offsets in radio source flux densities are expected to be a problem mainly for the FIRST survey, where significant amounts of flux of extended sources can be resolved out. Again, this problem only affects the normalization of the RLF, unless there is a redshift dependence in the amount of resolved-out flux. Since the results from the NVSS and FIRST radio data for the redshift evolution of the RLF from the maxBCG sample are consistent within statistical errors, we do not pursue this point further.

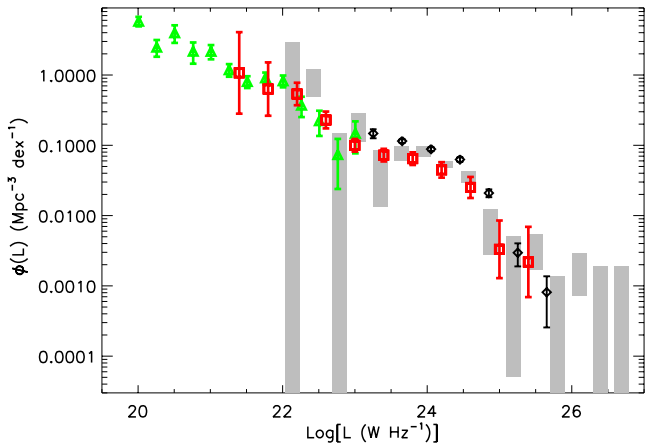

Fig. 9. Comparison of our RLF derived from the maxBCG/FIRST data in the lowest redshift bin ($0.1 < z < 0.17$, $z_{\rm median} = 0.13$; black diamonds) with other relevant volume-averaged radio luminosity functions. The RLF of Lin & Mohr (2007) is indicated by shaded regions, while the corresponding luminosity functions of Reddy & Yun (2004) and Massardi & De Zotti (2004) are shown as green triangles and red squares, respectively.

5.6. Comparison of the RLF with previous findings

To compare our findings with previously published results, we consider the maxBCG/FIRST data in our lowest redshift bin, which compares well to the low-redshift samples of galaxy clusters used in previous works. Figure 9 shows a comparison of our low-redshift RLF to the results of Lin & Mohr (2007), Reddy & Yun (2004) and Massardi & De Zotti (2004).

We note that the normalization of the RLF is consistent with the results of LM07, although the RLF from our optically selected sample does not extend as high in luminosity ($\mathrm{Log}(L) \gtrsim 26$ W Hz^{-1}). The latter is likely a result of the fact that the optically selected sample contains many more low-mass clusters, and that the more luminous radio sources tend to reside in high-mass clusters (cf. Sect. 5.4.1).

The RLF of Massardi & De Zotti (2004) has a significantly lower normalization than what we find, by approximately a factor of two. This can be expected due to the different definition of cluster volumes (using a constant cluster radius across the complete sample) used in the former work.

Branchesi et al. (2006) used a definition of the RLF as the number of radio sources per cluster rather than averaged over a volume. A direct comparison with that work would require a re-analysis of the Branchesi et al. (2006) sample, which would be only of moderate interest considering that the normalization would rely on different assumptions on cluster volume and the sample is selected differently from our maxBCG sample. Our main objective here is to show the approximate agreement between different local luminosity functions and to stress the difficulty in obtaining a robust normalization of the RLF; although the normalization depends strongly on the choice of cluster volume and is prone to systematic effects due to a poor understanding of this volume, this does not strongly affect our main conclusion, which is concerned with the redshift evolution of the RLF independently of its overall normalization.

Including systematic uncertainties, all our results are consistent with no number density evolution of the RLF with redshift. This result is compatible with the findings of Gralla et al. (2010), who detected no redshift evolution in the number of sources per unit of cluster mass for a sample of 618 optically selected clusters in the redshift range $0.35 < z < 0.95$.

Early studies of the luminosity function of optically selected QSOs at $z \leq 2.2$ suggested a pure luminosity evolution with $L \sim (1+z)^{(3.5\pm0.3)}$ in the field population (Boyle et al. 1987, 1988). A later study of extragalactic radio sources by Dunlop & Peacock (1990) at 2.7 GHz came to similar conclusions.

The pure luminosity evolution of the volume averaged RLF found in this study is approximately consistent with more recent findings in the field population of radio galaxies at low and intermediate redshift (Machalski & Godlowski 2000; Brown et al. 2001), although our best-fit evolutionary model with $L \sim (1+z)^{(6.20\pm1.76)}$ is steeper than both the $L \sim (1+z)^{(4\pm1)}$ found by Brown et al. (2001) and the $L \sim (1+z)^{(3\pm1)}$ which Machalski & Godlowski (2000) found to be consistent with their data.

6. Summary and conclusions

We used the maxBCG optical sample of galaxy clusters and a composite X-ray sample to construct the volume averaged radio luminosity function (RLF) in galaxy clusters by cross-correlating cluster positions with radio point source positions from the FIRST and NVSS survey catalogs. Background and foreground counts were corrected for, and variable confusion with redshift was accounted for. We investigated the radial source density distribution of radio sources associated with clusters, and correlated the luminosity of the brightest radio source with cluster mass.

To fit the radial number density distributions, we used the functional form of the isothermal β-model. Combining the maxBCG cluster sample with the FIRST catalog, we found an additional narrow component which we identify with radio detections of the brightest cluster galaxies (BCGs). All combinations of cluster sample (maxBCG or X-ray) and radio source sample (NVSS or FIRST) yield similar values of the power law index β. The core radius in the maxBCG/FIRST radial distribution of sources compares well to the distribution of sources in the X-ray sample. As it was not possible to identify the narrow BCG component from the NVSS survey, we found a much smaller core radius in the maxBCG/NVSS radial distribution.

Our derived radial distributions are narrower than what has been found in earlier studies (e.g. Reddy & Yun 2004; Massardi & De Zotti 2004), even when disregarding the central component associated with brightest cluster galaxies (BCGs). A plausible explanation is that we are constructing the RLF at higher redshifts than previous studies and thus, given our flux limit of 5 mJy, we are sensitive only to radio-loud AGN. At lower redshift there is a mixing with star forming galaxies, which have a less centralized distribution.

Unlike LM07, we do not find any evidence that bright radio sources have a radial source density distribution different from that of faint sources. Again, a likely explanation is that we are studying different populations of radio sources through the redshift selection.

We found that the luminosity of the most radio-luminous source within 50 kpc from the cluster center scales with cluster mass following a power law with slope 0.31 ± 0.12 in the maxBCG sample. This is consistent with the results of Lin & Mohr (2004) as well as with the results from our X-ray sample, although the latter is also consistent with no correlation.

We find the RLFs constructed from the optical and X-ray samples of galaxy clusters to be in approximate agreement. The RLF from the optical maxBCG sample is systematically lower at

luminosities $L \gtrsim 3 \times 10^{25}$ W Hz^{-1}. This is likely a result of many more low-mass systems being present in the optical sample.

We provide the first evidence for a luminosity evolution of the volume-averaged RLF in clusters of galaxies. The maxBCG/FIRST data are consistent with a pure luminosity evolution, with power scaling with redshift as $L \sim (1+z)^{\alpha_L}$, where $\alpha_L = 6.20^{+1.76+0.19}_{-1.76-0.17}$ (statistical followed by systematic uncertainties). There is no indication of a mass dependence in the RLF from the present data. However, the results from the X-ray sample are consistent with the findings of LM07, that the most luminous radio sources reside in massive clusters. This is further corroborated by the fact that the RLF constructed from the maxBCG sample (which contains a smaller fraction of high-mass systems than both our X-ray sample and the sample of LM07) is steeper at higher luminosities.

Below $P \sim 10^{25}$ W Hz^{-1}, the data are consistent with no mass dependence in the RLF, as shown by constructing the RLF in the low-redshift X-ray sample and binning by mass. Although we have found that massive clusters have more luminous BCGs, this effect is counteracted in the RLF by the fact that these massive systems also have more volume. Both the X-ray sample and the maxBCG sample yield results consistent with a pure luminosity evolution of the RLF. In addition, the derived power laws are comparable, although the samples cover very different redshift ranges.

Acknowledgements. We acknowledge partial support for this work from Priority Programme 1177 and Transregio Programme TR33 of the German Research Foundation (Deutsche Forschungsgemeinschaft). For the early stages of this work, M.W.S. acknowledges support through a stipend from the International Max Planck Research School (IMPRS) for Radio and Infrared Astronomy at the Universities of Bonn and Cologne. F.P. acknowledges support from grant 50 OR 1003 of the Deutsches Zentrum für Luft- und Raumfahrt. H.A. is grateful to Mexican CONACyT for research grants 50921-F and 118295.

References

Andreon, S., & Hurn, M. A. 2010, MNRAS, 404, 1922
Arnaud, M., & Evrard, A. E. 1999, MNRAS, 305, 631
Arnaud, M., Pointecouteau, E., & Pratt, G. W. 2005, A&A, 441, 893
Becker, M. R., McKay, T. A., Koester, B., et al. 2007, ApJ, 669, 905
Becker, R. H., White, R. L., & Helfand, D. J. 1995, ApJ, 450, 559
Best, P. N., von der Linden, A., Kauffmann, G., Heckman, T. M., & Kaiser, C. R. 2007, MNRAS, 379, 894
Birkinshaw, M. 1999, Phys. Rep., 310, 97
Böhringer, H., Voges, W., Huchra, J. P., et al. 2000, ApJS, 129, 435
Böhringer, H., Schuecker, P., Guzzo, L., et al. 2004, A&A, 425, 367
Boyle, B. J., Fong, R., Shanks, T., & Peterson, B. A. 1987, MNRAS, 227, 717
Boyle, B. J., Shanks, T., & Peterson, B. A. 1988, MNRAS, 235, 935
Branchesi, M., Gioia, I. M., Fanti, C., Fanti, R., & Perley, R. 2006, A&A, 446, 97
Brough, S., Couch, W. J., Collins, C. A., et al. 2008, MNRAS, 385, L103
Brown, M. J. I., Webster, R. L., & Boyle, B. J. 2001, AJ, 121, 2381
Burenin, R. A., Vikhlinin, A., Hornstrup, A., et al. 2007, ApJS, 172, 561
Cavaliere, A., & Fusco-Femiano, R. 1978, A&A, 70, 677
Coble, K., Bonamente, M., Carlstrom, J. E., et al. 2007, AJ, 134, 897
Condon, J. J. 1984, ApJ, 287, 461
Condon, J. J., Cotton, W. D., Greisen, E. W., et al. 1998, AJ, 115, 1693
Condon, J. J., Cotton, W. D., & Broderick, J. J. 2002, AJ, 124, 675
Cooray, A. R., Grego, L., Holzapfel, W. L., Joy, M., & Carlstrom, J. E. 1998, AJ, 115, 1388
Croft, S., de Vries, W., & Becker, R. H. 2007, ApJ, 667, L13
De Lucia, G., & Blaizot, J. 2007, MNRAS, 375, 2
Dunlop, J. S., & Peacock, J. A. 1990, MNRAS, 247, 19
Eastman, J., Martini, P., Sivakoff, G., et al. 2007, ApJ, 664, L9
Ebeling, H., Barrett, E., Donovan, D., et al. 2007, ApJ, 661, L33
Edge, A. C. 1991, MNRAS, 250, 103
Galametz, A., Stern, D., Eisenhardt, P. R. M., et al. 2009, ApJ, 694, 1309
Gehrels, N. 1986, ApJ, 303, 336
Gralla, M. B., Gladders, M. D., Yee, H. K. C., & Barrientos, L. F. 2010 [arXiv:1010.6011]
Haarsma, D. B., Leisman, L., Donahue, M., et al. 2010, ApJ, 713, 1037
Hart, Q. N., Stocke, J. T., & Hallman, E. J. 2009, ApJ, 705, 854
Ho, P. T. P., Altamirano, P., Chang, C., et al. 2009, ApJ, 694, 1610
Horner, D. J., Perlman, E. S., Ebeling, H., et al. 2008, ApJS, 176, 374
Johnston, D. E., Sheldon, E. S., Wechsler, R. H., et al. 2007 [arXiv:0709.1159]
Koester, B. P., McKay, T. A., Annis, J., et al. 2007, ApJ, 660, 239
Komatsu, E., Dunkley, J., Nolta, M. R., et al. 2009, ApJS, 180, 330
Kotov, O., & Vikhlinin, A. 2005, ApJ, 633, 781
Ledlow, M. J., & Owen, F. N. 1996, AJ, 112, 9
Lin, Y., & Mohr, J. J. 2004, ApJ, 617, 879
Lin, Y., & Mohr, J. J. 2007, ApJS, 170, 71 (LM07)
Lin, Y., Partridge, B., Pober, J. C., et al. 2009, ApJ, 694, 992
Machalski, J., & Godlowski, W. 2000, A&A, 360, 463
Mandelbaum, R., Seljak, U., & Hirata, C. M. 2008, J. Cosmol. Astro-Part. Phys., 8, 6
Martini, P., Sivakoff, G. R., & Mulchaey, J. S. 2009, ApJ, 701, 66
Massardi, M., & De Zotti, G. 2004, A&A, 424, 409
Muchovej, S., Leitch, E., Carlstrom, J. E., et al. 2010 [arXiv:1012.1610]
Reddy, N. A., & Yun, M. S. 2004, ApJ, 600, 695
Rozo, E., Rykoff, E. S., Evrard, A., et al. 2009a, ApJ, 699, 768
Rozo, E., Rykoff, E. S., Koester, B. P., et al. 2009b, ApJ, 703, 601
Rykoff, E. S., Evrard, A. E., McKay, T. A., et al. 2008a, MNRAS, 387, L28
Rykoff, E. S., McKay, T. A., Becker, M. R., et al. 2008b, ApJ, 675, 1106
Sarazin, C. L. 1988, X-ray emissions from clusters of galaxies, Cambridge Astrophysics Series (Cambridge: Cambridge University Press)
Schwan, D., Bertoldi, F., Cho, S., et al. 2003, New Astron. Rev., 47, 933
Sheldon, E. S., Johnston, D. E., Scranton, R., et al. 2009, ApJ, 703, 2217
Sivakoff, G. R., Martini, P., Zabludoff, A. I., Kelson, D. D., & Mulchaey, J. S. 2008, ApJ, 682, 803
Smith, R. K., Brickhouse, N. S., Liedahl, D. A., & Raymond, J. C. 2001, ApJ, 556, L91
Stocke, J. T., Perlman, E. S., Gioia, I. M., & Harvanek, M. 1999, AJ, 117, 1967
Sunyaev, R. A., & Zeldovich, Y. B. 1972, A&A, 20, 189
Vanderlinde, K., Crawford, T. M., de Haan, T., et al. 2010, ApJ, 722, 1180
Vikhlinin, A., McNamara, B. R., Forman, W., et al. 1998, ApJ, 502, 558
White, M. 2001, A&A, 367, 27
White, R. L., Becker, R. H., Helfand, D. J., & Gregg, M. D. 1997, ApJ, 475, 479